Original

Dankert, H.; Horstmann, J.; Rosenthal, W.:
Ocean wind fields retrieved from radar-image sequences.
In: Journal of Geophysical Research. Vol. 108 (2003) C 11, 3352.
First published online by AGU: 14.11.2003

http://dx.doi.org/10.1029/2003JC002056

Ocean wind fields retrieved from radar-image sequences

H. Dankert, J. Horstmann, and W. Rosenthal
Institute for Coastal Research, GKSS Research Center, Geesthacht, Germany

Received 18 July 2003; revised 3 September 2003; accepted 12 September 2003; published 14 November 2003.

[1] The dependency of radar backscatter on the surface wind field is investigated using a nautical X-band radar operating at grazing incidence and horizontal polarization in transmit and receive. This resulted in development of an algorithm for wind retrieval from nautical radar image sequences. The algorithm consists of two parts: In the first part, wind directions are extracted from wind-induced streaks that are in line with the mean surface wind direction. These streaks are visible in the temporal integrated radar images at scales between 100 and 500 m. The orientation of the streaks is determined from the local gradients, which are derived from the radar images smoothed and reduced to the appropriate scales. In the second part, wind speeds are derived from the backscatter of the temporal integrated radar image sequence and the radar retrieved wind direction. The dependency of the radar backscatter on the local surface wind and geometry of the radar is parameterized by training a neural network. The algorithm is applied to radar image sequences acquired by a nautical X-band radar mounted aboard an offshore platform in the North Sea. The radar-derived winds are validated by comparison to in situ wind data measured at the platform. The comparison of wind directions resulted in a correlation of 0.99 with a standard deviation of 14.2°; for wind speeds the correlation is 0.97 with a standard deviation of 0.85 m s^{-1}. In contrast to traditional offshore wind sensors, the retrieval of the wind field from the backscatter of the ocean surface makes the system independent of the sensors motion and installation height and reduces the effects due to platform-induced blockage and turbulence effects. *INDEX TERMS:* 4275 Oceanography: General: Remote sensing and electromagnetic processes (0689); 3360 Meteorology and Atmospheric Dynamics: Remote sensing; 3307 Meteorology and Atmospheric Dynamics: Boundary layer processes; 4504 Oceanography: Physical: Air/sea interactions (0312); *KEYWORDS:* real aperture radar, marine radar, wind, neural networks

Citation: Dankert, H., J. Horstmann, and W. Rosenthal, Ocean wind fields retrieved from radar-image sequences, *J. Geophys. Res.*, *108*(C11), 3352, doi:10.1029/2003JC002056, 2003.

1. Introduction

[2] Wind is a major driving force in ocean dynamics; it is responsible for the transfer of energy and momentum from the atmosphere to the ocean and supports the gas-exchange processes between the lower marine atmospheric boundary layer and upper ocean surface. Thus wind is a key parameter in the coupled atmosphere, ocean, and biosphere system. Measurements of ocean winds are performed using various different methods, for example, in situ by anemometers (point measurements through time), and by remote sensing with scatterometers (spatial measurements). In situ measurements are mainly collected by ships and buoys of which the first are affected by blockage effects and variable mast heights and the latter by tilt and displacement height, especially in high winds and sea states. The remote sensing techniques require excellent calibration as well as model functions that parameterize the dependence of the backscatter on the wind and have a rather coarse resolution.

0148-0227/03/2003JC002056

[3] In this paper a radar-based remote sensing technique is introduced, which enables the measurement of the ocean surface wind from towers and ships. Therefore a nautical radar operating at X-band is used that has the capability of measuring the backscatter from the ocean surface in space and time under most weather conditions, independent of light conditions. Biases of wind measurements, due to tilt and height variation, as well as due to the sensor motion, do not exist. Also, the blockage as well as the turbulence effects due to the sensor platform are strongly reduced and, in case of tower-based measurements, are considered in the algorithm.

[4] In addition to the wind retrieval presented here, nautical radar image sequences of the sea surface are also used to determine other hydrographic parameters. In particular, they have been used to determine two-dimensional wave-spectra and significant wave heights [*Borge et al.*, 1999], individual wave parameters [*Borge et al.*, 2003], wave groups [*Dankert et al.*, 2003a], the near-surface current [*Senet et al.*, 2001], and bathymetry [*Bell*, 1999; *Trizna*, 2001]. Recently, new methods for the current and bathymetry field retrieval from the nautical radar image sequences have been developed [*Dankert*, 2003].

[5] It is well known that the local wind field generates the small-scale roughness of the sea surface, which in turn raises the radar backscatter of the ocean surface [*Lee et al.*, 1995; *Trizna*, 1997]. The radar cross section (RCS) of the sea surface is strongly dependent on the local wind speed [*Lee et al.*, 1996] and angle between the antenna viewing direction and wind direction (H. Hatten et al., Azimuthal and range dependency of sea-surface radar backscatter at HH-polarization and low grazing incidence, submitted to *IEEE Transactions on Geoscience and Remote Sensing*, 2003) (hereinafter referred to as Hatten et al., submitted manuscript, 2003). This dependency enables the deduction of the wind vector from radar images of the sea surface. In the presence of long surface waves, the small-scale surface roughness, and subsequently the radar backscatter, is modulated. At moderate incidence angles the modulation is mainly due to the tilt and hydrodynamic modulation [*Alpers et al.*, 1981], while at grazing incidence the modulation stems also from the shadowing of the radar beam due to the ocean waves [*Wetzel*, 1990]. These modulation mechanisms lead to the imaging of surface waves whose wavelength are greater than two times the radar resolution.

[6] Several studies on the wind dependency of radar data acquired at grazing incidence have already been performed [*Chaudhry and Moore*, 1984; *Lee et al.*, 1996; Hatten et al., submitted manuscript, 2003]. In these studies the dependency of the RCS on wind speed and direction has been investigated. Hatten et al. (submitted manuscript, 2003) showed that the spectral noise of X-band HH-polarized radar images is correlated with the wind speed and wind direction. *Keller et al.* [1985] have studied the dependency of the RCS on air-sea temperature difference and sea state [*Keller et al.*, 1994]. For a detailed description of scattering at low grazing incidence, refer to *Wetzel* [1995] and *Brown* [1998].

[7] In this paper a new algorithm is proposed to retrieve ocean winds from nautical radar-image sequences. The algorithm consists of two parts; in the first, wind directions are retrieved from wind-induced streaks, which are imaged by the radar at scales of approximately 100 to 500 m, using a method based on derivation of local gradients [*Horstmann et al.*, 2002; *Koch*, in press, 2003]. This method has already been successfully applied for wind direction retrieval from space-borne synthetic aperture radar (SAR) images [*Horstmann et al.*, 2002]. In the second part, the dependency of the RCS on wind is parameterized by training a neural network (NN). NNs have been used in several applications in remote sensing, for example, derivation of water properties from imaging spectrometers [*Schiller and Doerffer*, 1999], as well as for wind retrieval from scatterometer (SCAT) [*Richaume et al.*, 2000] and SAR data [*Horstmann et al.*, 2003]. In addition to the wind dependency of the RCS, the dependency on the air-sea temperature difference is considered in the wind retrieval algorithm.

[8] The paper is organized as follows: In section 2 the radar system and available data are introduced. Section 3 shows the dependency of the radar image intensity on wind speed and direction. In section 4 the wind direction retrieval algorithm is introduced and applied to the radar data sets. The determined wind directions are compared to in situ data recorded at the radar platform. In section 5, NNs are introduced and applied to wind speed retrieval from the radar-image sequences. The radar retrieved wind speeds are compared to the in situ measurements collected at the platform. Finally, in section 6, conclusions and an outlook are given.

2. Investigated Data

[9] The utilized radar system consists of a typical nautical radar and a WaMoS II unit, which allows for the continuous digitization of time series of polar nautical radar images. The nautical radar was operated at 9.5 GHz (X-band) with horizontal (HH) polarization in transmit and receive at grazing incidence in a height of 74 m over mean sea level. For wind retrieval the radar covers an area within a radius of $\approx$2000 m with an antenna-revolution time of $\approx$2.5 s. The spatial resolution at a distance of $\approx$750 m from the antenna is $\approx$10 m in range and $\approx$12 m in azimuth. Several WaMoS II systems are operated on an operational basis aboard towers and ships in the North Sea to measure wave parameters. However, the 4 months of investigation of radar-image sequences from February to June 2001, representing 3271 acquisition times, were recorded at the Norwegian platform Ekofisk 2/4 k located $\approx$200 km off the west coast of Norway in the North Sea. Each image sequence consists of 32 images, representing a time span of $\approx$80 s.

[10] Nautical radar systems are equipped with a logarithmic amplifier and are not radiometrically calibrated. Therefore the normalized RCS could not be determined. The backscattered signal of each radar resolution cell is digitized with 8 bit, which allows gray values between 0 (no backscatter) and 255 (highest signal).

[11] In Figure 1, the platform, the location of the installed radar system, and a recorded sample radar-image sequence are shown. The radar antenna is installed at the northwest corner of the platform marked by the white arrow. The radar-image sequence shows a wave field, which is propagating in northeast direction. The dark patches in the radar images are due to the platform equipment, for example, the helicopter deck and the lattice towers. The higher backscatter in the south originates from the other platforms of the oilfield, which are also visible in the background of the photograph. For the investigations, only areas representing backscatter from the sea surface are considered. The ranging patterns in the near range are caused by multiple reflections of the antenna side lobes in the near field from the host platform equipment in a distance of about 500 m, due to the longer running time of the radiated energy. To neglect this effect, the investigations have been performed beginning at 900-m range.

[12] For comparison, wind measurements were collected by a wind anemometer and a wind vane, mounted at a height of 80 m above sea level at Ekofisk 2/4 k. The in situ wind speeds are 10-min means and are converted to 10 m height. In addition, the air and water temperatures as well as significant wave heights and peak periods were collected at Ekofisk 2/4 k with a wave rider buoy beside the platform.

3. Wind Dependence on the Radar Cross Section

[13] It is well known that the backscatter of the ocean surface is primarily caused by the small-scale surface roughness, which is strongly influenced by the local wind

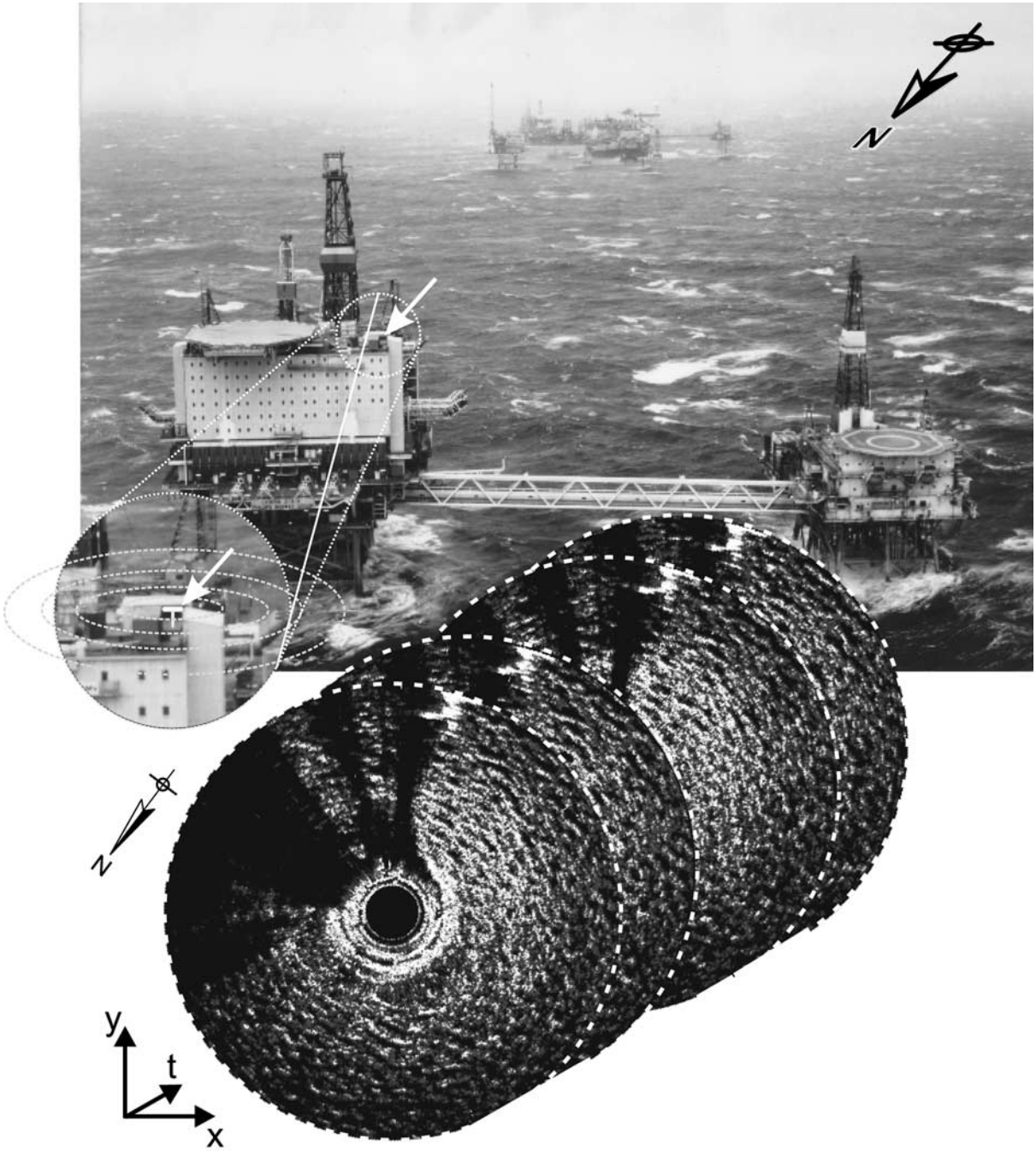

Figure 1. Ekofisk 2/4 k platform of the Ekofisk oil field in the North Sea. The WaMoS system is installed at the northwest corner of the platform. In the radar images, several shadows are visible, which are due to the equipment of the platform. The large backscatter in the south originates from the oil field visible in the background of the photo.

field and therefore allows the backscatter to be empirically related to wind. Measurements at grazing incidence indicate that the backscatter at grazing incidence with HH polarization results from small-scale breaking waves as scattering elements [*Lee et al.*, 1995; *Wetzel*, 1995; *Trizna*, 1997; *Brown*, 1998]. The RCS of the ocean surface, σ, is related to the near-surface wind speed u and antenna-look direction versus wind direction, $\Delta\Phi = \Phi_{radar} - \Phi_{wind}$,

$$RCS = a \cdot u^{\gamma}(1 + b \cdot \cos\Delta\Phi), \quad (1)$$

whereas $\Delta\Phi$ is defined here as 180° looking up-wind. The coefficients a, b and γ generally depend on radar frequency, polarization, and incidence angle.

[14] By integrating a radar-image sequence over time (typically 32 images representing 1 min of data), signatures with higher variability in time (like surface waves) are averaged out. Only static patterns such as the shadows from the towers and the wind signatures remain visible in the mean RCS $\bar{\sigma}$. The hypothesis is that $\bar{\sigma}$ depends on the wind direction and wind speed, whereas the temporal and spatial

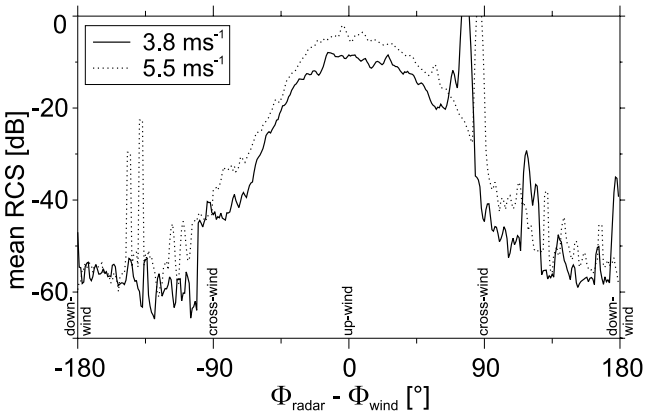

Figure 2. Wind direction in respect to radar look direction versus range-integrated RCS for different wind speeds. The data were acquired from a tower-based radar in the Odra Lagoon at the German coast of the Baltic Sea.

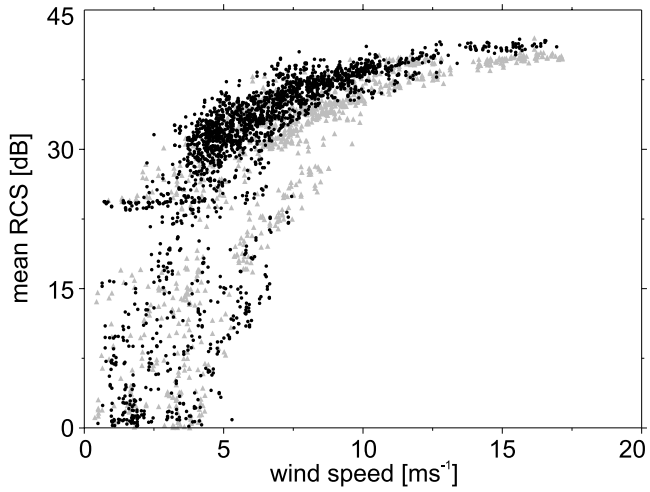

Figure 3. Scatterplot of in situ wind speed versus mean RCS. Black dots represent mean RCS from data sets acquired at wind directions between 170° and 40°, while shaded triangles represent data between 40° and 170°.

variability of the backscatter distribution is mainly due to the local wave field modulation. Both processes show an azimuthal dependency.

[15] In Figure 2 the wind direction, with respect to the radar look direction, is plotted versus the mean RCS in range for a wind speed of 3.8 and 5.5 m s^{-1}. The radar image sequences were acquired by a similar radar system installed in the Odra lagoon at the German coast of the Baltic Sea in summer 1997. In this setup the radar images were not affected by shadows caused by equipment. Furthermore, the RCS was not modulated by ocean waves, due to the very limited fetch and very shallow water depth in this area. The two curves show that the RCS has its maximum when the antenna is viewing in up-wind direction ($\Delta\Phi = 0°$) and has a minimum when viewing in down-wind direction ($\Delta\Phi = \pm 180°$). This result for X-band with HH polarization is in accordance with results of *Trizna and Carlson* [1996] and Hatten et al. (submitted manuscript, 2003). The single peak stands in contrast to radar measurements of the sea surface in X-band with VV polarization and radars operating at moderate incidence angles where two maxima are observed, one at up-wind and one at down-wind [*Trizna and Carlson*, 1996; *Hatten et al.*, 1998]. Local minima are here at cross wind. The up-wind RCS is slightly higher than the down-wind one. The single peak makes radar measurements obtained with HH polarization at grazing incidence the best choice for wind direction measurements, because they enable the retrieval of unambiguous wind directions (refer to section 4).

[16] Figure 3 shows the scatterplot of in situ wind speeds converted to 10 m height versus mean RCS of each of the radar image sequences. The mean RCS was retrieved from the total image sequence excluding the masked area shown in Figure 4. There is a strong dependency of the mean RCS on wind speeds over the entire range of wind speeds. A group of outliers (shaded triangles) can be identified with a shift of the RCS toward lower intensities. These outliers belong to radar sequences where the wind direction was between 40° and 170°. In these cases the upwind peak of radar backscatter is expected to be located in the masked area, which was neglected in retrieval of the mean RCS and therefore leads to a lower mean RCS than expected.

4. Wind Direction Retrieval

[17] The wind direction retrieval is based on wind-induced streaks, which are visible in the mean radar image resulting from integration of the radar-image sequence over time. The wind-induced streaks are aligned in wind direction and have a typical spacing of 100 to 500 m. They are most likely caused by features such as local turbulences, streaks from foam, or surfractants that are aligned with the mean surface wind direction. Wind-induced streaks have

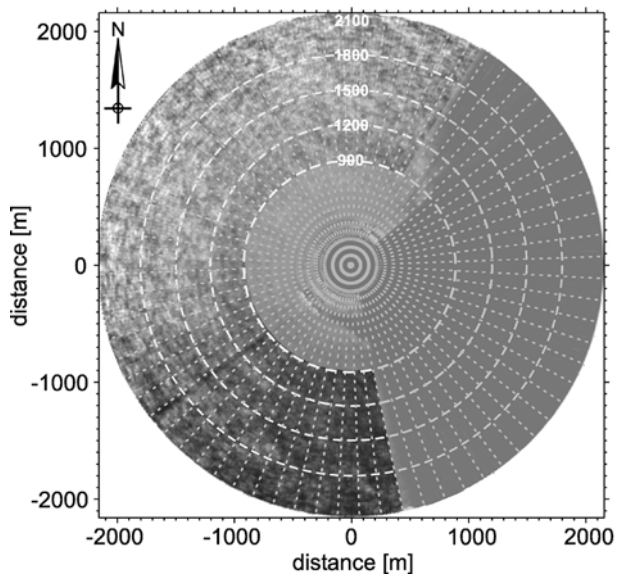

Figure 4. Mean RCS of a radar-image sequence of 32 images from Ekofisk 2/4 k. The masked area was not considered for the wind retrieval. The polar image is divided into subareas in range (300 m) and azimuth (5°).

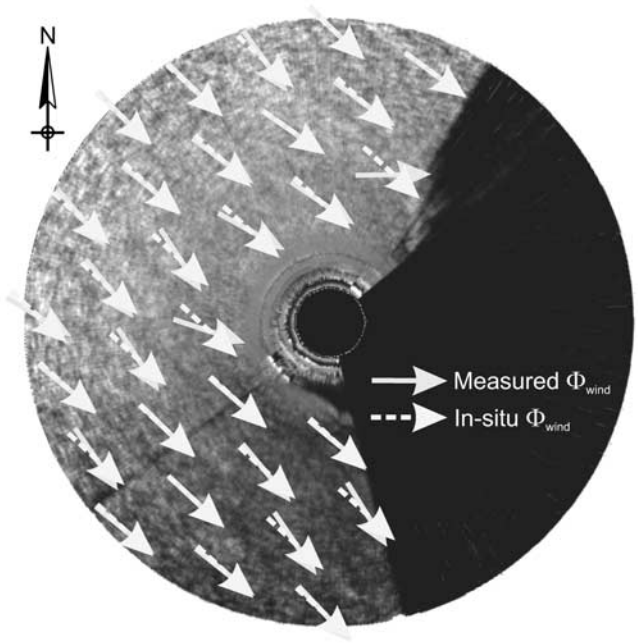

Figure 5. Mean RCS of a radar-image sequence from Ekofisk 2/4 k on April 15, 2001. The wind speed was 8 m s^{-1}, and the measured wind direction at 74 m height (dashed arrows) was 335°. Superimposed are solid arrows giving the retrieved local wind direction at the ocean surface.

also been observed in satellite-borne SAR imagery at similar [*Horstmann et al.*, 2002] and larger scales [*Gerling*, 1986] and are used to retrieve the wind direction [*Lehner et al.*, 1998; *Horstmann et al.*, 2002; *Wackerman et al.*, 2003]. In the following, wind-induced streaks are assumed to be approximately in line with the mean wind direction.

[18] The orientation of wind-induced streaks is normal to the local gradients derived from smoothed amplitude images. To retrieve the local gradients, the mean RCS image is iteratively smoothed and sub-sampled to obtain a so-called Gaussian pyramid. From level to level the resolution decreases by a factor of 2; the RCS image size decreases correspondingly to a pixel size of 20, 40, and 80 m. From these pixels the local directions are computed with a 180° directional ambiguity. The wind directions resulting from the different pixel sizes vary typically only by a few degrees, except for cases where additional features are present. A detailed description of the local gradient based algorithm for retrieval of wind induced streaks is given by *Koch* [in press, 2003].

[19] In principle, the 180° directional ambiguity could be removed searching for the upwind peak in the mean polar image (see Figure 2). However, most radar installations do not allow the recording of the backscatter from the ocean surface over the entire azimuth (entire revolution of antenna). Often the radar is affected by platform equipment that leads to disturbed areas in the polar radar image (Figure 1) and therefore in difficulties finding the upwind peak. This is especially the case for radar systems based at the coast as well as for systems aboard oil rigs such as the setup of Ekofisk 2/4 k.

[20] In this case the 180° directional ambiguity is removed by extracting the movement of wind gusts visible in the radar image sequence. The radar image sequence is subdivided into two or more sub-sequences (typically 24 images), which may overlap each other in time. Each sub-sequence is then integrated over time to remove signatures with higher temporal variability such as ocean surface waves. From these mean RCS images the movement of wind gusts is retrieved. A standard technique to estimate the shift of moving image patterns between two data takes is to compute the cross-correlation function (CCF). The respective propagation distance is indicated by the location of the CCF peak. Alternatively, the shift can also be estimated looking at the cross spectrum (CS), which is defined as the Fourier spectrum of the CCF. In the CS the shift of the different harmonic waves in the image is given by the respective phases of the complex valued CS. The directions resulting from the CS are always within 90° of the in situ measured wind direction and therefore enables the 180° directional ambiguity left open by the local gradient method to be resolved. The same results can be achieved using differential-based motion estimation techniques [*Jähne et al.*, 1999], which enable the retrieval of the movement of the mean RCS at each pixel [*Dankert et al.*, 2003b]. Also in this case the mean resulting direction is within 90° of the in situ measured wind direction. However, the latter method requires significantly longer computation times.

[21] In Figure 5 the mean RCS image resulting from the image sequence is shown. Superimposed onto the radar image are the wind directions resulting from the 240-m pixel layer of the local gradient retrieval scheme (solid arrows) and the in situ measurements (dashed arrows). It can be seen that both measurements agree well.

[22] In Figure 6 the scatterplot of the comparison of wind directions measured in situ and by the radar system is given. In this case the radar wind direction for each measurement

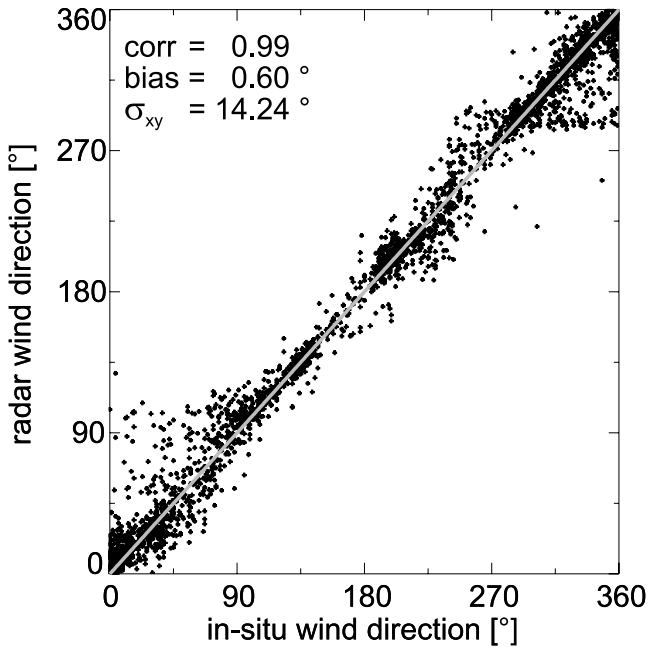

Figure 6. Scatterplot of in situ wind directions versus radar-derived wind directions.

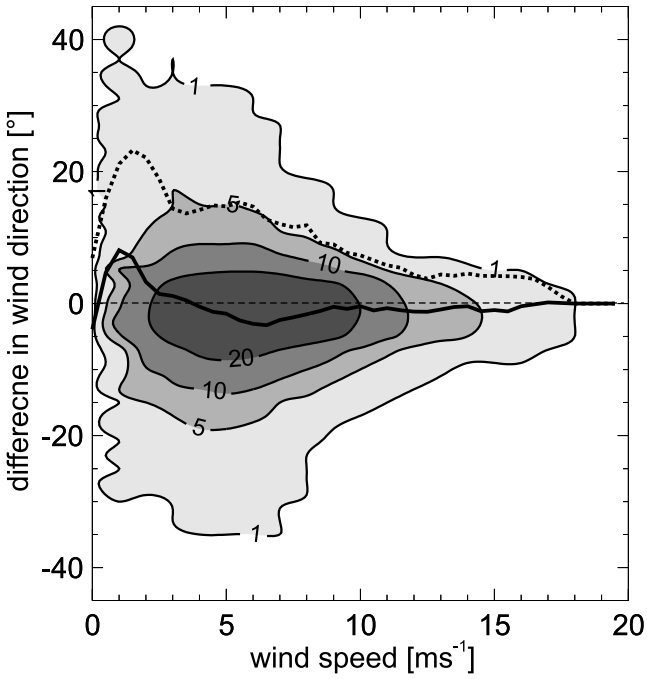

Figure 7. Scatterplot of wind speeds versus difference between radar and in situ wind directions. The solid and dotted lines give the bias and standard deviation, respectively.

represents the mean of all determined local wind directions. The scatterplot considers all of the 3271 image sequences. The standard statistical parameters result in a correlation of 0.99, a bias of 0.6°, and a standard deviation of 14°.

[23] In Figure 7, wind speed is plotted versus wind direction differences resulting from radar and in situ wind directions. Superimposed are the bias (solid line) and standard deviation (dotted line) in dependence on wind speed. The dependence of the bias on wind speed is negligible; however, the standard deviation decreases significantly with increasing wind speed.

[24] Slightly larger errors were obtained from satellite-borne SAR imagery, where wind directions were retrieved from streaks at scales above 400 m and compared to in situ measurements [*Vachon and Dobson*, 1996; *Lehner et al.*, 1998; *Fetterer et al.*, 1998] as well as to numerical model results [*Horstmann et al.*, 2002]. The comparison of SAR-derived wind directions retrieved at different scales [*Wackerman et al.*, 2003] indicate that the smaller scales used here are better suited for wind direction retrieval.

5. Wind Speed Retrieval Using Neural Networks

[25] A straightforward method for retrieving wind speeds from uncalibrated radar images can be obtained by using a NN. The NN approach does not require explicit models for the radar imaging process and can therefore be easily applied to any system configuration, that is, polarization, incidence angle, etc. The only requirements for application of a NN to radar-wind speed retrieval is the relative radiometric stability of the system as well as a dependency of backscatter on wind speed. In the case of the system aboard Ekofisk 2/4 k, both requirements are fulfilled (section 3). In the following, feed-forward backpropagation NNs (http://gfesun1.gkss.de/software/ffbp) are used as a multiple nonlinear regression technique to parameterize the relationship between the radar intensity and ocean surface wind.

[26] A NN is built up of several layers: an input layer, one or more hidden layers, and one output layer. Each layer consists of "neurons"; the input layer has as many neurons as input parameters, and the output layer has as many neurons as output parameters. The number of hidden layers and number of neurons in the hidden layer(s) is dependent upon the problem. Each neuron in a layer is linked to each neuron of the neighboring layer with a weight.

[27] An example of a NN with two hidden layers is given in Figure 8. The output value N_{out} of each neuron is derived according to

$$N_{\text{out}} = S\left(-N_{\text{bias}} + \sum_{i=1}^{n} w_i x_i\right), \tag{2}$$

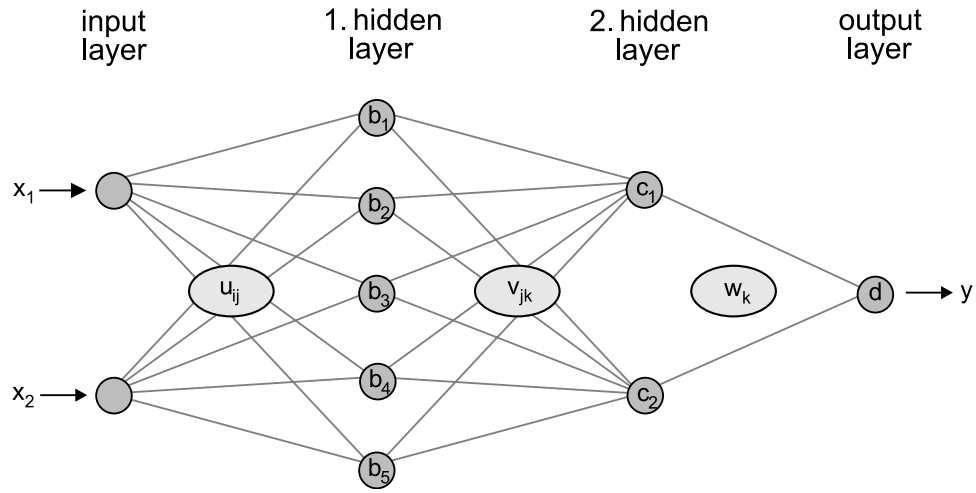

Figure 8. Schematic of a neural network (NN) having two input parameters, two hidden layers with five and two neurons, and an output layer with one parameter.

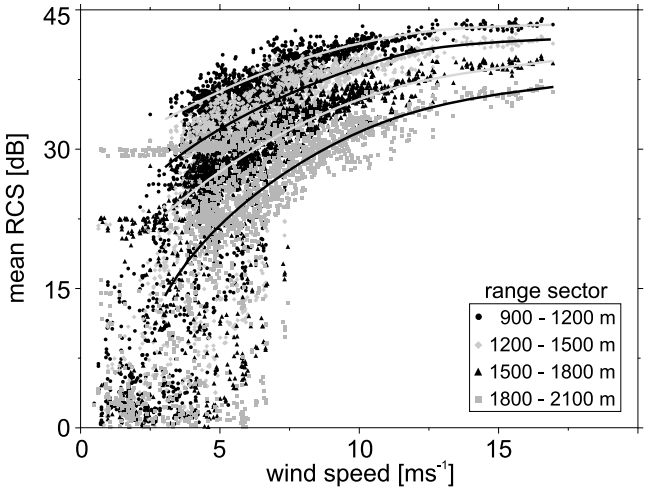

Figure 9. In situ measured wind speed is plotted versus mean RCS of the range sectors for each of the 3271 analyzed data sets. The curves were fitted to each of the range sectors.

where N_{bias} is a bias value specific to each neuron, n is the number of incoming links, w is a weight specific to each neuron, x is the output value of the neuron in the preceding layer, and S is a nonlinear function assuming monotonically increasing values between zero and one as the value of the argument goes from $-\infty$ to ∞. The most common choice, also used in the NNs applied here, is the sigmoid function $[1 + \exp(-x)]^{-1}$. A NN operates sequentially from layer to layer; output neurons of the first layer are given by the input values. The output of each neuron of the first hidden layer is computed by the summation of the weighted inputs, shifting by the bias and application of the nonlinear function. This is repeated for each layer until the output layer is reached, giving the results of the NN. To determine a NN, a sufficiently large set of input and output vectors has to be available to generate a training and a test sample. During the training of the NN, the values of the biases and weights are changed to minimize the error function. The resulting trained NN has to be tested with the test sample for its generalization power, for example, whether reasonable results are produced for input values, which are not included in the training sample.

[28] To take into account the dependencies of the RCS on wind direction and range distance, the mean RCS image (integrated over time) was subdivided in several range and azimuth bins. The range was subdivided into four 300-m intervals starting at 900 m and the azimuth was subdivided into 5° bins. For each bin, the mean RCS was retrieved.

[29] The four range partitions were implemented to extend the sensitivity of the sensor on wind speed. The utilized radar system is only equipped with an 8-bit analogue to digital convertor and therefore saturation can occur for higher wind speeds especially in near range. In Figure 9 the in situ measured wind speed is plotted versus the mean RCS of the range bins for each of the 3271 data sets. The superimposed curves were fitted to the points of each range bin. As expected, the RCS decreases with range. However, more important for the wind speed retrieval is the change of sensitivity on wind speeds with range. In the near range (900–1200 m) the sensitivity RCS on wind speed is higher at low wind speeds, while in the far range (1800–2100 m) the sensitivity is larger for high wind speeds. For this reason, the utilization of the mean RCS from the different range sectors enables a significantly better parameterization for the entire range of wind speeds.

[30] For the training of NNs, all areas affected by shadows due to the platform equipment, the backscatter from neighboring platforms, and the near range of up to 720 m from the radar antenna were neglected. The ratio between the training and test data set was set to 2:1.

[31] In a first step, NNs were trained using the RCS of each of the four range bins and the mean radar retrieved wind direction in respect to the antenna look direction as input and the in situ measured anemometer wind speed converted to 10 m height as output. Several different NNs were trained using all range-azimuth bins and range-azimuth bins within ±15° upwind and/or down wind direction, as well as range-azimuth bins within ±15° of cross-wind directions. The best result was found for the NN trained with the wind directions within ±15° of both cross-wind directions. This is due to the highest wind sensitivity at cross wind and due to artifacts caused by the neighboring platforms such as wind shadowing in the downwind case and blockage in the upwind case.

[32] In a second step, NNs were trained with the RCSs of the four range bins in cross-wind direction, the wind direction versus north, and the radar look direction versus north as input and the wind speed at 10 m height as output. The resulting NN is composed of three hidden layers with six neurons in the first, five in the second, and four in the third hidden layer. Comparison to the prior NN shows a significant improvement concerning the main statistical parameters shown in Table 1.

[33] This improvement is due to the dependence of the RCS on the radar look direction versus north, which is caused by side effects due to objects around the platform such as wind shadowing due to the large platform array south of Ekofisk 2/4 k. For example, in Figure 10 the wind blows from 141° with 14.5 m s^{-1}. It can be seen that in the lee of the platform the backscatter of the ocean surface is significantly reduced in comparison to its surrounding, which is the wind shadowing effect of the platforms (arrows in Figure 10).

[34] It is well know that the stratification conditions in the lower marine atmospheric boundary layer (MABL), mainly denoted by the air-sea temperature difference, affect the stability of the air-sea interface and therefore also the wind profile. In turn, the wind profile influences the radar backscatter of the ocean surface. This leads at equivalent wind speeds in 10 m height to a higher radar backscatter of the ocean surface in case of an unstable MABL than for neutral and stable conditions [*Keller et al.*, 1989]. For this

Table 1. Main Statistical Parameters Resulting From the NNs Considering the Different Input Data

Input Data Set	Correlation	Bias	σ_{xy}
RCS, $\Delta\Phi_{(radar,wind)}$	0.95	0.03	1.11
RCS, Φ_{radar}, Φ_{wind}	0.96	0.01	0.97
RCS, $\Delta\vartheta_{(air,sea)}$, $\Delta\Phi_{(radar,wind)}$	0.96	0.03	0.95
RCS, $\Delta\vartheta_{(air,sea)}$, Φ_{radar}, Φ_{wind}	0.97	0.03	0.85

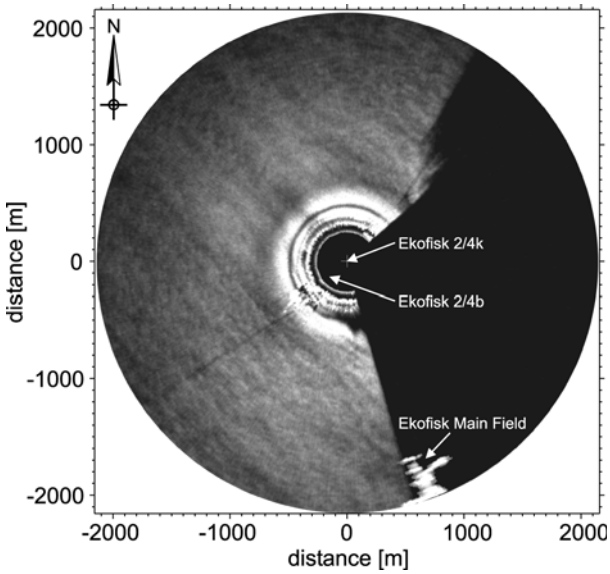

Figure 10. Wind shadowing due to the Ekofisk main field and Ekofisk 2/4 b,k.

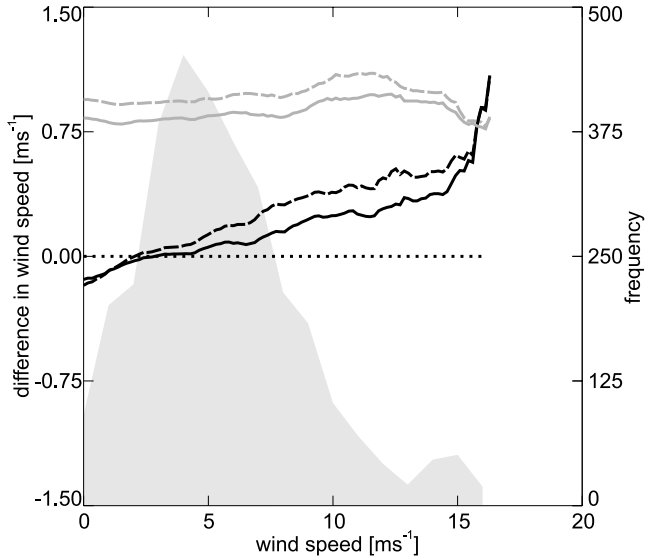

Figure 12. Bias (black curves) and standard deviation (shaded curves) in wind speed of comparisons of anemometer wind speeds to radar wind speeds for intervals of 0.2 m s^{-1} for Figure 11a (dashed curve) and Figure 11b (solid curve). In addition, the histogram of wind speeds is plotted.

reason, in a third step, a NN was trained considering, in addition to the NN trained in the second step, the air-sea temperature differences. The resulting NN consists of three hidden layers with six neurons in the first, five neurons in the second, and four neurons in the third hidden layer. Again, the main statistical parameters improve compared to the previously trained NNs, resulting in a correlation of 0.97, a negligible bias, and a standard deviation of 0.85 m s^{-1} (see Table 1).

[35] In Figure 11, in situ wind speeds are plotted against the wind speed resulting from nautical radar images using the last two NNs. The corresponding statistics of the comparison are given in the upper left of the scatterplots. Figure 11a gives the result of the second NN, which did not find a dependency on wind speeds below ≈2 m s^{-1}. In Figure 11b the results of the third NN (including air-sea temperature differences) are shown, which enable the retrieval of wind speeds as low as ≈0.75 m s^{-1}.

[36] In Figure 12, the bias (black lines) and the standard deviation (shaded lines) in wind speed of the comparisons

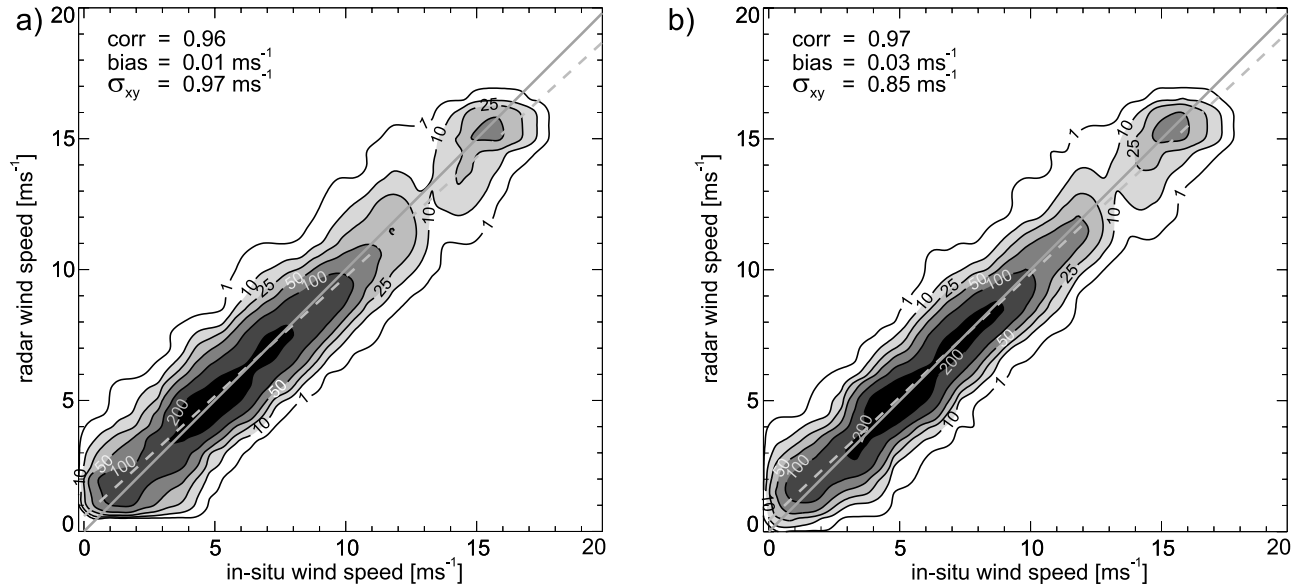

Figure 11. Scatterplots giving the comparison of the wind anemometer wind speeds (mean of 10 min) versus wind speeds retrieved from colocated nautical radar images. The radar wind speeds were retrieved in both cases using a NN with the intensity of the mean radar image and the wind direction from the colocated anemometer data as input. In (Figure 11b, additionally, the air-sea temperature difference has been considered for NN training.

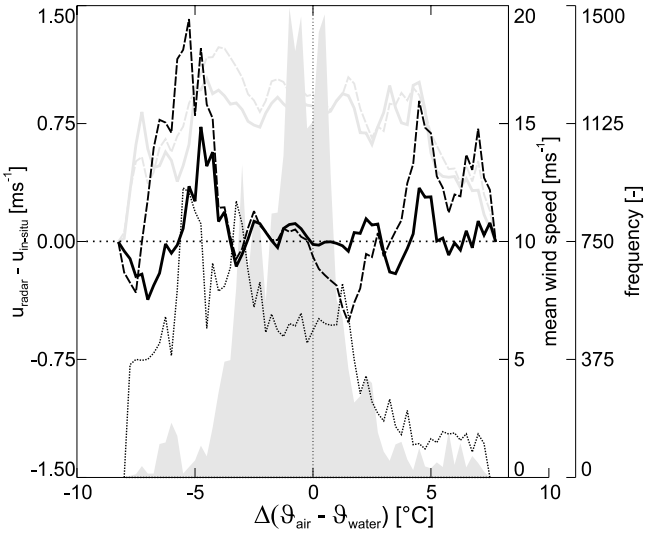

Figure 13. Bias (black curve) and standard deviation (shaded curve) of radar retrieved wind speeds (with/without considered air-sea temperature difference (solid/dashed curves)) and in situ wind speeds over air-sea temperature difference. The dotted black curve gives the mean wind speed for each air-sea temperature difference bin. A histogram (shading) of all training/test data sets is plotted.

of anemometer wind speeds to radar wind speeds are plotted for intervals of 0.2 m s^{-1} for the NNs considered in Figure 11a (dashed line) and Figure 11b (solid line). In addition, a histogram of wind speeds is plotted. For wind speeds below 8 m s^{-1}, the bias is very low and the standard deviation is rather constant. Above 8 m s^{-1}, the bias increases significantly, which is due to the insufficient number of available data at higher wind speeds for the training of NNs. Comparing both NNs improves both statistical parameters when considering air-sea temperature differences.

[37] To show the importance of the stratification conditions, the bias and standard deviation of the difference between radar and in situ wind speed are plotted against the air-sea temperature difference (Figure 13). Additionally, the mean wind speed for each air-sea temperature difference bin (dotted curve) and a histogram (shading) of all training and test data is given. For very unstable air-sea interfaces, there is a high bias for the NN without considering the air-sea temperature difference (dashed curve). The NN is overestimating the wind speed, because with an unstable MABL, the RCS is larger than for a stable one. In the transition region the agreement is very good. For weakly stable conditions, the NN is underestimating the wind speed, which corresponds to a decreasing RCS with increasing $\Delta\vartheta$. This is in agreement with theory and the observations of *Keller et al.* [1989]. For very stable conditions, the radar wind speeds are higher. This is explained with the nature of the NN, which has no information about the stratification conditions. Therefore it is averaging the low-speed occurrences that also happened under unstable conditions with those under stable conditions. The result is an overestimation of radar wind speeds. Therefore the knowledge of the stratification conditions together with radar measurements is important. Considering the air-sea temperature difference results in an improvement of the bias for both the unstable and the stable conditions. The standard deviation is similar for both NNs.

6. Conclusions and Outlook

[38] The RCS of the ocean surface at X-band with HH polarization at grazing incidence is strongly dependent on the surface wind speed, wind direction, range distance, and air-sea temperature differences. This provides the opportunity to develop an algorithm for remote measurements of the surface wind vectors from radar images. The resulting algorithm consists of two steps; one for wind direction and another for wind speed retrieval.

[39] Wind directions are retrieved from wind-induced streaks, which are oriented in wind direction and have a typical spacing of 100 to 500 m. The streak orientations are deduced by retrieving the local gradients of the mean RCS image, which results from integration of the radar image sequence over time as well as iterative smoothing and subsampling of the image. The resulting wind direction has a 180° ambiguity, which is removed by extracting the movement of wind gust patterns visible in the radar image sequence. Comparison to in situ measurements acquired at the radar platform and converted to 10 m height gave a correlation of 0.99 with a bias of 0.6° and a standard deviation of 14.2°. It was also found that the wind direction retrieval accuracy increases with wind speed.

[40] Wind speeds are retrieved from the dependence of the RCS on wind speed and wind direction. To parameterize the dependency of the RCS on the wind, NNs were trained considering different input parameters. Owing to the missing radiometric calibration of the radar, the NNs have to be trained for each setup. The minimal parameters needed as input to the NN are the mean RCSs in cross-wind direction at four different ranges, together with the radar retrieved wind direction in respect to the antenna look direction. It was found that cross wind is the best choice because the wind field is not disturbed by the platform itself. To take into account the dependence of the RCS on the stability in the lower MABL, the air-sea temperature difference has to be taken as additional input to the NN, showing a significant improvement of the wind speed retrieval. The latter is the best choice for radar setups aboard ships or platforms which are standing alone well off the coast. If the radar platform is situated at the coast or in the neighborhood of a larger object, for example, another platform, the input of wind direction to the NN has to be differentiated. This allows the influence of the platform's neighborhood on the wind field to be taken into account, for example, wind shadowing due to another platform. In the case of the data available from the Platform Ekofisk 2/4 k, the best results were obtained with input of the mean RCSs in cross-wind direction at four different ranges, air-sea temperature differences, and the radar retrieved differentiated wind direction. In comparison to in situ wind speeds measured at the platform and converted to 10 m height, the correlation is 0.97 with a bias of 0.03 m s^{-1} and a standard deviation of 0.85 m s^{-1}.

[41] It is not always possible to set up temperature sensors to measure the air-sea temperature difference, for example, on ship-borne installations. Comparing the plots in Figure 11 shows that the parameterization without implemented air-

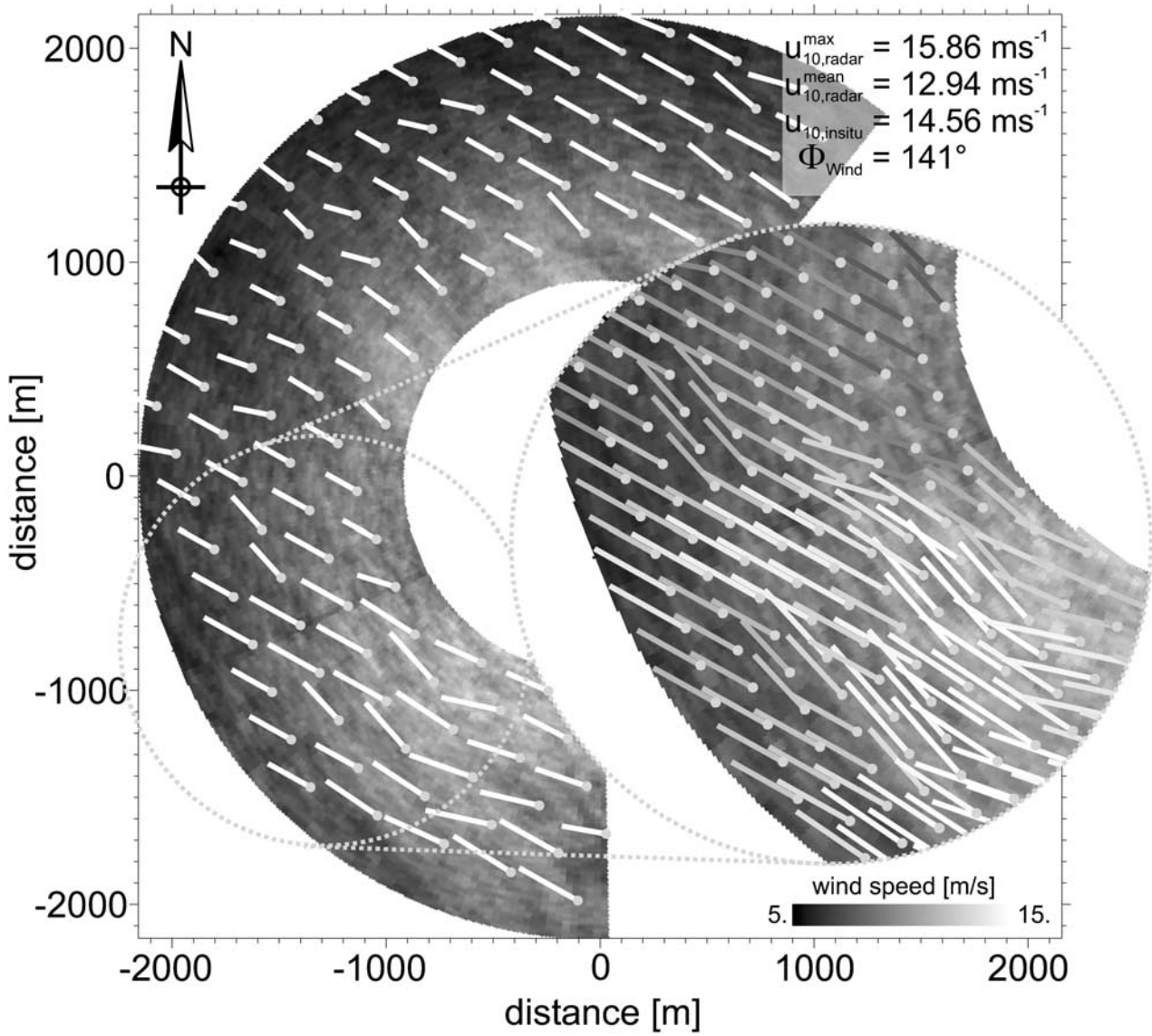

Figure 14. High-resolution ocean wind field retrieved at Ekofisk 2/4 k on March 27, 2001, using the determined local wind directions together with an NN that parameterizes the wind speed spatially.

sea temperature information already gives very good and practicable results. The radar system can therefore be installed without any other additional sensors for wind measurements. In contrast to typical in situ sensors like anemometers, the measurements of the radar system are not influenced by movements of ships or platforms and local turbulences due to installations.

[42] The method is extended to retrieve high-resolution wind fields from the radar image sequences. The wind directions are retrieved from the wind-induced streaks via local gradients with a resolution of 120 m. For the wind speeds, a NN was trained considering the mean RCS and distance to antenna, as well as wind direction and antenna look direction versus north. Figure 14 shows the resulting wind field with a resolution of 240 m in case of the whole radar image as well as 120 m concerning the cutout.

[43] In future, more data sets from Ekofisk 2/4 k will be considered for the purpose of investigating a larger bandwidth of wind speeds for improving the results and finding the limitations of the radar system. Hatten et al. (submitted manuscript, 2003) could show that for 23 m s^{-1}, no saturation occurs. Furthermore, the wind-induced streaks are used to retrieve wind vectors locally, spatially, and temporally [*Dankert et al.*, 2003b].

[44] **Acknowledgments.** The authors were supported by the Bundesministerium für Bildung und Forschung (BMBF) in the framework of the ENVOC project (contract 01SF9918/8) and by the European Commission in the framework of European project MaxWave (contract 3-2000-00544). All radar image sequences were kindly made available by the company Oceanwaves, Lueneburg, Germany. The authors would like to thank Anne-Karin Magnusson (Norwegian Meteorological Institute, Bergen, Norway) for providing the in situ data. We owe thanks to Helmut Schiller (GAS Research Center, Geesthacht, Germany) for providing routines for training of NNs.

References

Alpers, W. R., D. B. Ross, and C. L. Rufenach, On the detectability of ocean surface waves by real and synthetic aperture radar, *J. Geophys. Res.*, *86*, 6481–6498, 1981.

Bell, P. S., Shallow water bathymetry derived from an analysis of X-band marine radar images of waves, *Coastal Eng.*, *37*, 513–527, 1999.

Borge, J. N., K. Hessner, and K. Reichert, Estimation of the significant wave height with x-band nautical radars, *Proceedings of the 18th International Conference on Offshore Mechanics and Arctic Engineering* (*OMAE*), *OMAE99/OSU-3063*, Am. Soc. of Mech. Eng. (ASME Int.), St. John's, Newfoundland, Can., 1999.

Borge J. N., G. R. Rodríguez, K. Hessner, and P. I. González, Inversion of nautical radar images for surface wave analysis, *J. Atmos. Oceanic Technol.*, in press, 2003.

Brown, G. S., Special issue on low-grazing angle backscatter from rough surfaces, *IEEE Trans. Antennas Propag.*, *46*, 1–161, 1998.

Chaudhry, A. H., and R. K. Moore, Tower based backscatter measurements of the sea, *IEEE J. Oceanic Eng.*, *9*, 309–316, 1984.

Dankert, H., Retrieval of surface-current fields and bathymetries using radar-image sequences, paper presented at International Geoscience Remote Sensing Symposium, Inst. of Elect. and Elect. Eng., Toulouse, France, 2003.

Dankert, H., J. Horstmann, A. K. Magnusson, and W. Rosenthal, Ocean winds retrieved from X-band radar-image sequences, paper presented at International Geoscience Remote Sensing Symposium, Inst. of Elect. and Elect. Eng., Toulouse, France, 2003a.

Dankert, H., J. Horstmann, S. Lehner, and W. Rosenthal, Detection of wave groups in SAR images and radar-image sequences, *IEEE Trans. Geosci. Remote Sens.*, *41*, 1437–1446, 2003b.

Fetterer, F., D. Gineris, and C. Wackerman, Validating a scatterometer wind algorithm for ERS-1 SAR, *IEEE Trans. Geosci. Remote Sens.*, *36*, 476–492, 1998.

Gerling, T. G., Structure of the surface wind field from Seasat SAR, *J. Geophys. Res.*, *91*, 2308–2320, 1986.

Hatten, H., F. Ziemer, and J. Seemann, and J. C. Nieto-Borge, Correlation between the spectral background noise of a nautical radar and the wind vector, paper presented at 17th International Conference on Offshore Mechanics and Arctic Engineering (OMAE), Am. Soc. of Mech. Eng. (ASME Int.), Lisboa, Portugal, 1998.

Horstmann, J., W. Koch, S. Lehner, and R. Tonboe, Ocean winds from RADARSAT-1 ScanSAR, *Can. J. Remote Sens.*, *28*, 524–533, 2002.

Horstmann, J., H. Schiller, J. Schulz-Stellenfleth, and S. Lehner, Global wind speed retrieval from SAR, *IEEE Trans. Geosci. Remote Sens.*, in press, 2003.

Jähne, B., H. Haußecker, and Peter Geißler, *Handbook of Computer Vision and Applications*, Academic, San Diego, Calif., 1999.

Keller, W. C., W. J. Plant, and D. E. Weissman, The dependence of X band microwave sea return on atmospheric stability and sea state, *J. Geophys. Res.*, *90*, 1019–1029, 1985.

Keller, W. C., V. Wismann, and W. Alpers, Tower-based measurements of the ocean C band radar backscattering cross section, *J. Geophys. Res.*, *94*, 924–930, 1989.

Keller, W. C., W. J. Plant, R. A. Petitt, and E. A. Terray, Microwave backscatter from the sea: Modulation of received power and Doppler bandwidth by long waves, *J. Geophys. Res.*, *99*, 9751–9766, 1994.

Koch, W., Directional analysis of SAR images aiming at wind direction, *IEEE Trans. Geosci. Remote Sens.*, in press, 2003.

Lee, P. H. Y., J. D. Barter, K. L. Beach, C. L. Hindman, B. M. Lake, H. Rungaldier, J. C. Shelton, A. B. Williams, R. Lee, and H. C. Yuen, X-band microwave backscattering from ocean waves, *J. Geophys. Res.*, *100*, 2591–2611, 1995.

Lee, P. H. Y., J. D. Barter, E. Caponi, M. Caponi, C. L. Hindman, B. M. Lake, and H. Rungaldier, Wind-speed dependence of small-grazing-angle microwave backscatter from sea surfaces, *IEEE Trans. Antennas Propag.*, *44*, 333–340, 1996.

Lehner, S., J. Horstmann, W. Koch, and W. Rosenthal, Mesoscale wind measurements using recalibrated ERS SAR images, *J. Geophys. Res.*, *103*, 7847–7856, 1998.

Richaume, P., F. Badran, M. Crepon, C. Mejia, H. Roquet, and S. Thiria, Neural network wind retrieval from ERS-1 scatterometer data, *J. Geophys. Res.*, *105*, 8737–8751, 2000.

Schiller, H., and R. Doerffer, Neural network for emulation of an inverse model: Operational derivation of case II water properties from MERIS data, *Int. J. Remote Sens.*, *20*, 1735–1746, 1999.

Senet, C. M., J. Seemann, and F. Ziemer, The near-surface current velocity determined from image sequences of the sea surface, *IEEE Trans. Geosci. Remote Sens.*, *39*, 492–505, 2001.

Trizna, D. B., A model for Brewster angle effects on sea surface illumination for sea scatter studies, *IEEE Trans. Geosci. Remote Sens.*, *35*, 1232–1244, 1997.

Trizna, D. B., Errors in bathymetric retrievals using linear dispersion in 3-d FFT analysis of marine radar ocean wave imagery, *IEEE Trans. Geosci. Remote Sens.*, *39*, 2465–2469, 2001.

Trizna, D. B., and D. J. Carlson, Studies of dual polarized low grazing angle radar sea scatter in nearshore regions, *IEEE Trans. Geosci. Remote Sens.*, *34*, 747–757, 1996.

Vachon, P. W., and F. W. Dobson, Validation of wind vector retrieval from ERS-1 SAR images over the ocean, *Global Atmos. Ocean Syst.*, *5*, 177–187, 1996.

Wackerman, C., J. Horstmann, and W. Koch, Operational estimation of coastal wind vectors from RADARSAT SAR imagery, paper presented at International Geoscience Remote Sensing Symposium, Inst. of Elect. and Elect. Eng., Toulouse, France, 2003.

Wetzel, L. B., Electromagnetic scattering from the sea at low grazing angles, in *Surface Waves and Fluxes*, vol. II, edited by G. L. Geernaert and W. J. Plant, pp. 109–171, Kluwer Acad., Norwell, Mass., 1990.

Wetzel, L. B., Sea clutter, in *Radar Handbook*, Addison-Wesley, Reading, Mass., 1995.

H. Dankert, J. Horstmann, and W. Rosenthal, Institute for Coastal Research, GKSS Research Center, Max-Planck-Strasse 1, Building 11, D-21502 Geesthacht, Germany. (dankert@gkss.de; horstmann@gkss.de; rosenthal@gkss.de)